# Modeling Interference for the Coexistence of 6G Networks and Passive Sensing Systems

Paolo Testolina, *Student Member, IEEE*, Michele Polese, *Member, IEEE*, Josep M. Jornet, *Senior Member, IEEE*, Tommaso Melodia, *Fellow, IEEE*, Michele Zorzi, *Fellow, IEEE* 

Abstract—Future wireless networks and sensing systems will benefit from access to large chunks of spectrum above 100 GHz, to achieve terabit-per-second data rates in 6th Generation (6G) cellular systems and improve accuracy and reach of Earth exploration and sensing and radio astronomy applications. These are extremely sensitive to interference from artificial signals, thus the spectrum above 100 GHz features several bands which are protected from active transmissions under current spectrum regulations. To provide more agile access to the spectrum for both services, active and passive users will have to coexist without harming passive sensing operations. In this paper, we provide the first, fundamental analysis of Radio Frequency Interference (RFI) that large-scale terrestrial deployments introduce in different satellite sensing systems now orbiting the Earth. We develop a geometry-based analysis and extend it into a data-driven model which accounts for realistic propagation, building obstruction, ground reflection, for network topology with up to  $10^5$  nodes in more than 85 km<sup>2</sup>. We show that the presence of harmful RFI depends on several factors, including network load, density and topology, satellite orientation, and building density. The results and methodology provide the foundation for the development of coexistence solutions and spectrum policy towards 6G.

# I. INTRODUCTION

Continuously growing user demand is pushing the 6G of wireless networks into the sub-terahertz (Sub-THz) spectrum of 100-300 GHz [1]. The Sub-THz spectrum offers theoretically orders of magnitude greater bandwidth than typical communication bands depending on the composition of the atmosphere and weather conditions [2]. This makes Sub-THz attractive for wireless networks, despite the significant challenges related to blockage, low transmission power, and small antenna apertures, which require directional antennas to increase the Next Generation Node Base (gNB) coverage [3].

However, this portion of the spectrum is already used by remote (passive) sensing systems in Earth Exploration-Satellite Service (EESS) and radio astronomy, supporting the weather, climate, and astronomy enterprises. Such services can tolerate limited to no interference. For this reason, the spectrum above 100 GHz features a set of channels reserved for passive remote sensing. This results in 12.5 GHz being the largest contiguous bandwidth available for communications under 200 GHz under current spectrum regulations [4]. Without sharing portions of the spectrum between EESS and the Sub-THz terrestrial communication systems, there is little benefit in climbing all

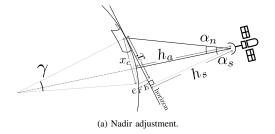
P. Testolina and M. Zorzi are with the Department of Information Engineering, University of Padova, Padova, Italy. Email: {testolina,zorzi}@dei.unipd.it. M. Polese, J. M. Jornet, and T. Melodia are with the Institute for the Wireless Internet of Things, Northeastern University, Boston, MA. Email: {m.polese, j.jornet, melodia}@northeastern.edu. The work of P. Testolina was supported by Fondazione CaRiPaRo under grants "Dottorati di Ricerca" 2019. This work also partially funded by NSF with award CNS-2225590.

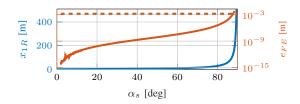
the way from 71 GHz into Sub-THz or terahertz (THz) bands, if the resulting bandwidth will be comparable. Hence, channels wider than 12.5 GHz are very much desired. Further, larger chunks of microwave and Sub-THz spectrum can also benefit passive sensing systems themselves, e.g., for more precise hyper-spectral remote sensing [5]. The same applies to radio astronomy, to sense molecular shifts in bands outside those traditionally allocated for this use [4].

Therefore, today's fixed spectrum allocation is limiting the potential of both communications and remote sensing. While this could be true across the entire radio spectrum, the much more challenging propagation of Sub-THz and THz signals through the atmosphere and the opportunity to more precisely control the radiation with compact antenna structures opens the door to more flexible spectrum sharing strategies [4], [6], [7]. To date, however, the literature presents a gap in the modeling and analysis of the RFI caused by terrestrial next-generation wireless networks to EESS systems, as most analyses focus on single-link evaluations, simplified terrestrial network models, and tractable but simplified channel models [4], [7]. Modeling RFI is key to the development of tailored coexistence techniques. This is a timely need for the passive sensing and Sub-THz networking communities, as RFI insights can influence 6G standardization and next-generations of remote sensing systems, allowing coexistence embedded in the technology rather than layered on top as an afterthought.

In this paper, we fill this gap with the first analysis of 6G terrestrial RFI to passive sensing systems, based on a large-scale network model (with up to  $10^5$  nodes in more than  $85~\rm km^2$ ) and actual sensors deployed on multiple EESS missions. Our contributions are as follows:

- We model the channel with aggregated interference, ground reflections, terrestrial and EESS sensors beam patterns, building obstructions, and Sub-THz spreading and absorption losses, extending ITU models with deployment-specific details. Our model is extremely scalable and can also be used to analyze and model Non Terrestrial Networks (NTNs).
- We analyze the single-link interference probability, and show how the peculiar geometry of the terrestrial-satellite RFI setup can lead to significant interference from the ground reflection due to the combination of the terrestrial and satellite beam gains.
- We extend this into a data-driven large-scale simulation with multiple satellites (i.e., TEMPEST-D and the Microwave Limb Sounder (MLS) [8], [9]) and device deployments and obstructions based on OpenStreetMap (OSM) and 3D models, including urban cellular and backhaul. The area size and the number of buildings





(b) 2D-distance from the ground node to the reflection point (blue) and corresponding flat-Earth approximation error (orange) for different look-angles for a satellite at 400 km altitude and a ground node at 10 m from the ground.

Fig. 1: Schematic representation of the geometry of the system (a) and error due to the flat-Earth approximation (b).

(62512 3D polygons) are unprecedented and showcase how we can model large-scale, site-specific deployments.

• We show that dense Sub-THz networks can affect EESS satellites operations. Specifically, (i) even User Equipments (UEs) can generate harmful interference, when combined in large numbers; (ii) the secondary reflections (e.g., the ground reflection), although generating lower interference, are significant and not to be neglected; (iii) the attenuation outside the main lobe of directional arrays might not be enough to protect the passive users; whereas (iv) path loss and atmospheric attenuation as well as the building obstruction can shield them more effectively.

Therefore, there exist regimes in which interference is significant, and other conditions in which it does not lead to any harm to passive satellites. These insights are a starting point for (i) the design of 6G networks; (ii) passive/active sharing, based on an accurate RFI understanding; and (iii) data-driven spectrum policy toward 6G.

### II. RELATED WORKS

RFI analyses follow two main approaches. Single-link analysis considers the RFI generated by a single interferer and a single victim [4], [7], [10], [11]. Specifically, [12] was among the first studies to numerically characterize RFI at sub-THz frequencies. [4] analyzes it in several scenarios for a single backhaul, terrestrial link. Similarly, [7] considers an urban scenario where a receiver on a rooftop is used as a surrogate for the satellite. The overall attenuation is measured for different ground transmitter locations. The authors of both studies conclude that, for a single link in an urban area, harmful interference can be avoided if the satellite or the beam direction remains below certain angles.

The second approach relies on Monte Carlo simulations to aggregate interference from multiple interferers modeled through multiple random variables. RFI statistics are derived through multiple iterations. [13], [14] consider a Fixed Satellite Service (FSS) terrestrial station and compute the aggregated interference produced by the gNBs of a nearby network at 3.4-3.6 GHz and 18 GHz. The authors of [15] analyze the impact of automotive radars on satellite radiometers in the 22-27 GHz frequency range, and conclude that most realistic vehicle densities would generate harmful RFI. The authors of both studies conclude that coexistence between the two systems at millimeter wave (mmWave) frequencies is possible, provided that the base station deployment and configuration respect some conditions. [13], [16], [17] consider

random deployments of the gNBs and UEs, realistic antenna and beamforming radiation patterns, and stochastic channel models [18]. [19] provides an analysis of the interference between terrestrial and satellite relays in the 25.25-27.5 GHz bands, considering Line-of-Sight (LoS) propagation and the ITU channel model, and aggregating the interference over extremely wide areas  $(0.5^{\circ} \times 0.5^{\circ}$  latitude/longitude). The authors of [20] estimate the aggregated RFI distribution from a Fast Switching (FS) network to an aircraft at 18 GHz. In [21]–[23], the coexistence between terrestrial networks and EESS at mmWave frequencies is analyzed. In these papers, the building blockage and attenuation, the node locations, and the beamforming orientation are modeled through random variables, that are not representative of a real topology.

Obstruction by physical obstacles is indeed another key element for RFI, particularly at high frequencies. [24] stochastically estimates the aggregated interference from a wide area for the upper 6 GHz band using building statistics from real data for the city of Milan. This paper aims at filling these gaps in the literature, characterizing the RFI at sub-THz frequencies with the following original contributions: (i) we propose and validate a ray-based channel model that can scale to footprintwide areas; (ii) we use it to take a ray-tracing-like approach to an unprecedented scale, in terms of the number of terrestrial nodes, considered area, and building modeling; (iii) thanks to these elements, we analyze in detail the contribution of the multi-path component, in particular of the ground reflection, at the network level; (iv) we perform this analysis using real 3D building models and node distributions.

#### III. PROPAGATION MODEL

In this section, we extend the channel models from [25], [26] to improve their scalability and to embed key elements of propagation at frequencies above 100 GHz. We model the propagation through two paths: the direct or LoS ray and the ray reflected by the ground (Ground Reflection (GR)), to provide key insights on the multipath contribution to the overall RFI at the satellite. Thus, the ray power takes into account (a) the reflection loss (for the reflected ray); (b) the free-space spreading loss; (c) the "atmospheric" loss due to the molecular absorption of the atmosphere layers crossed by the ray; and (d) the absorption loss due to obstacles.

#### A. Ground-to-Satellite Path

The traditional 2-ray model [25] is based on the flat-Earth assumption when considering short distances. The effect of

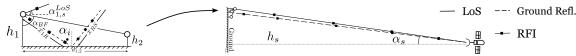


Fig. 2: Geometry of the problem (not to scale).

this simplification has been evaluated in several works [27]–[31]. However, the distance between the satellite and the ground node can be hundreds of kilometers not only on the altitude but also on the longitudinal plane. Here, we verify whether the flat-Earth assumption holds when considering the path reflected on the ground from the terrestrial node to the satellite.

Consider a satellite at altitude  $h_a$ , which points the main lobe of its sensor towards the ground with an angle  $\alpha_n$  with respect to nadir. By definition, the nadir at a given point is the direction pointing toward the center of the Earth. As shown in Fig. 1a, we distinguish between the *nadir* angle  $\alpha_n$ , i.e., the angle between the pointing direction and nadir, and the apparent nadir angle  $\alpha_s$  seen from the ground, i.e., the angle between the pointing direction of the satellite and the normal to the horizon. The relation between the two angles can be expressed as [32]

$$\alpha_s = \arcsin\left(\frac{r}{R}\sin\alpha_n\right),\tag{1}$$

where R is the Earth radius and  $r=R+h_a$  is the distance of the satellite from the center of the Earth, here assumed to be a perfect sphere for simplicity. Thus, a satellite at the horizon, with  $\alpha_s=90^\circ$ , has a nadir angle  $\alpha_n=\arcsin\left(\frac{R}{r}\right)$ , that for a satellite at  $h_a=400$  km of altitude corresponds to about  $70.21^\circ$ . Conversely, the same satellite looking at a  $65^\circ$  angle with respect to nadir has an apparent look-angle  $\alpha_s=74.41^\circ$ .

From  $\alpha_s$  it is straightforward to derive the incidence angle  $\alpha_i$ , the LoS angle  $\alpha_{1,s}^{LoS}$  between the ground node and the satellite, the distance  $x_{1R}$   $(x_{RS})$  between the ground node (satellite) and the reflection point, and the overall length of the reflected path x:

$$\alpha_i = \arctan\left(\frac{h_s}{h_s + h_1} \tan \alpha_s\right) \simeq \alpha_s$$
 (2)

$$\alpha_{1,s}^{LoS} = \arctan\left(\frac{h_s - h_1}{(h_s + h_1)\tan\alpha_i}\right) + \frac{\pi}{2}$$
 (3)

$$\simeq \arctan\left(\frac{1}{\tan\alpha_s}\right) + \frac{\pi}{2} = \pi - \alpha_s$$
 (4)

$$x_{1R} = h_1 \tan \alpha_i \qquad x_{RS} = h_s \tan \alpha_i$$

$$x_{GR} = x_{1R} + x_{RS}$$
(5)

We define the flat-Earth error at distance x from node 1 as  $e_{FE}(x) = |h_{FE}(x) - h_E(x)|$ , where  $h_{FE}(x)$  and  $h_E(x)$  are the flat and spherical Earth ground height at distance x, respectively. The error can be computed as  $e_{FE}(x) = x^2 + x_c^2 - 2xx_c\cos\left(\frac{\gamma}{2}\right)$ , where  $x_c = 2R\sin\left(\frac{\gamma}{2}\right)$  and  $\gamma = \arctan\left(\frac{x}{R}\right)$  are defined as in Fig. 1a. Fig. 1b shows the distance  $x_{1R}$  (blue) of the reflection point from the ground node, and the corresponding flat-Earth error  $e_{FE}(x_{1R})$ , for a ground node at 10 m and a satellite at 400 km altitude at different look-angles  $\alpha_s$ . As long as the satellite is above the horizon  $(\alpha_s < 80^\circ)$ , the ray is reflected on the ground closer

than 30 m from the ground node, a distance small enough so that the flat-Earth approximation holds, with an error in the order of  $10^{-5}$  m. For  $\alpha_s > 80^\circ$ , the reflection point is so far from the ground node that the curvature of the Earth needs to be accounted for. In that case, the approximations for the reflected path do not hold, whereas the model for the LoS remains valid. However, since in this work we are interested in analyzing also the effect of multipath, we limit our analysis to elevation angles  $\alpha_s \leq 80^\circ$ .

## B. Ray Power

As represented in Fig. 2, in our channel model we consider the direct ray (j = 0: LoS) and the ray reflected on the ground (j = 1), representing the two main propagation paths from the source to the receiver. Each ray is associated with a path loss  $L_j$  that depends on a number of elements, detailed in the following paragraphs.

a) Reflection Loss: If the ray j is reflected, a reflection loss  $L_{R,j}$  is applied, which changes with the incidence angle, with the polarization of the wave, and with the material of the reflecting surface. In this paper, we consider the reflection loss presented in [26], derived from [33].

The Fresnel reflection coefficients  $r_{TE}$  and  $r_{TM}$  model the power loss in the specular direction when the wave is reflected on a smooth surface for the Transverse Electric (TE) and Transverse Magnetic (TM) polarized waves, respectively. We present only the derivation for TE-polarized waves, without polarization loss, as the formulation for the TM mode is analogous. The reflection coefficient  $r = r_{TE}$  can be computed, considering the refraction index n and the absorption coefficient  $\alpha$ , as

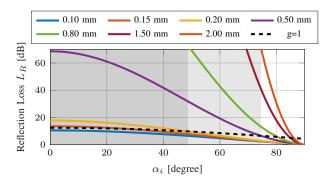
$$r = \frac{\cos \alpha_i - n\sqrt{1 - \left(\frac{1}{n}\sin \alpha_i\right)^2}}{\cos \alpha_i + n\sqrt{1 - \left(\frac{1}{n}\sin \alpha_i\right)^2}} = |r| e^{j\phi_R}$$
 (6)

where  $n=\sqrt{\epsilon}$  is the refractive index and  $\phi_R$  is the phase shift that occurs during the reflection. Relative permittivity coefficients  $\epsilon\in\mathbb{C}$  for common building materials in the frequency range of interest are reported in [34]. For simplicity, throughout this work we assume that  $\phi_R=\pi$ , i.e., r=-|r|.

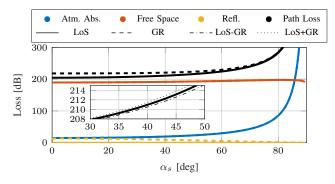
When considering outdoor propagation, particularly at high frequencies, reflections occur on rough materials, where scattering becomes relevant. To include the scattering loss in the specular direction, we multiply the Fresnel coefficient by the Rayleigh roughness factor

$$L_{R,j} = (\rho \cdot r)^{-1}$$
, with  $\rho = e^{-\frac{g}{2}}$ , (7)

where the roughness g of the material ( $g \ll 1$ : smooth,  $g \simeq 1$  moderately rough, g > 1 very rough) is defined as  $g = \left(\frac{4\pi\sigma\cos\alpha_i}{\lambda}\right)^2$ , where  $\sigma$  is the standard deviation of the surface roughness [33]. Note that the dependence of g on the incident angle  $\alpha_i$  accounts for the effective roughness



(a) Reflection loss  $L_R$  at 178 GHz for different values of the standard deviation  $\sigma$  of the surface roughness. g=1 (black dashed) marks the separation between rough and smooth surfaces, as confirmed by the much greater losses for  $\sigma>0.20$  mm.



(b) Contribution of the different losses at 178 GHz for a satellite at 400 km of altitude, for different elevation angles  $\alpha_s$  of the satellite. The free-space loss dominates, with the atmospheric absorption dominating when the satellite is at the horizon and the signal crosses a larger section of the atmosphere.

Fig. 3: Analysis of the reflection loss (a) and of the overall path loss with the individual contributions (b).

seen by the incoming wave. Fig. 3a reports the reflection loss as a function of the incident angles for different values of  $\sigma$ , computed with the relative permittivity for the concrete  $\epsilon = 5.24$  [34], that is used throughout the rest of this work.

b) Free-Space Loss: As the j-th ray propagates through the space, the signal is attenuated proportionally to the distance  $d_j$  and to the center frequency  $f_c$ . The free-space loss for ray j is thus computed as

$$L_{fs,j} = \frac{4\pi f_c d_j}{c}. (8)$$

Clearly, the LoS path is the shortest, with length  $d_0 < d_j, j \in \mathbb{N}^+$ . The length difference  $\Delta d$  between the LoS and the ground-reflected ray is approximated for the case of ground-to-satellite propagation in Eq. (9). An approximation for the phase difference in the two-ray model commonly adopted in the literature [25] is  $\Delta d \simeq 2\frac{h_1h_s}{x}$ , which holds when  $x\gg h_1+h_s$ . However, in the considered case, this assumption is not verified, and the approximation is not valid. Thus, we derived an approximation that can be applied to satellite communication:

$$\Delta d = \sqrt{x^{2} + (h_{1} + h_{s})^{2}} - \sqrt{x^{2} + (h_{s} - h_{1})^{2}} =$$

$$= \frac{x^{2} + (h_{1} + h_{s})^{2} - (x^{2} + (h_{s} - h_{1})^{2})}{\sqrt{x^{2} + (h_{1} + h_{s})^{2}} + \sqrt{x^{2} + (h_{s} - h_{1})^{2}}}$$

$$= \frac{4h_{1}}{\sqrt{\left(\frac{x}{h_{s}}\right)^{2} + \left(\frac{h_{1}}{h_{s}} + 1\right)^{2}} + \sqrt{\left(\frac{x}{h_{s}}\right)^{2} + \left(1 - \frac{h_{1}}{h_{s}}\right)^{2}}}$$

$$= \frac{4h_{1}}{\sqrt{\left(\frac{x}{h_{s}}\right)^{2} + 1} + \sqrt{\left(\frac{x}{h_{s}}\right)^{2} + 1}}$$

$$= \frac{2h_{1}}{\sqrt{\left(\frac{x}{h_{s}}\right)^{2} + 1}} = \frac{2h_{1}}{\sqrt{\left(\tan\left(\alpha_{s}\right)\right)^{2} + 1}}$$
(9)

where the approximation holds for  $h_s \gg h_1$ , which applies to ground-to-satellite scenarios.

Fig. 3b compares the path loss of the direct and of the reflected ray. Note from Eq. (9) that  $\Delta d$  varies between 0 (satellite at the horizon) and  $2h_1$  (satellite directly above the ground node), that makes the difference between the free-space loss of the two paths negligible.

c) Atmospheric Loss: Electromagnetic waves propagating through the atmosphere interact with the molecules, transferring part of their energy to the medium. This effect is accounted for through the atmospheric absorption coefficient  $L_{A,j}$ , which depends on the composition of the atmospheric layers and on the propagation angle of the j-th ray [4], [6]:

$$L_{A,j} = \left( \int_0^{h_a} \frac{\gamma(h)}{\sqrt{1 - \cos^2(\theta(h))}} \, \mathrm{d}h \right)^{-1} \tag{10}$$

where  $\gamma(h) = \gamma_o(h) + \gamma_w(h)$  is the attenuation given by oxygen  $(\gamma_o)$  and water vapor  $(\gamma_w)$  at height h,  $h_a$  is the satellite altitude, and  $\theta(h)$  is the local apparent elevation angle at height h.

d) Absorption Loss: In the sub-THz bands, the transmitted power through materials is negligible [35]. Thus, for large obstacles, e.g., buildings, with multiple, thick, non-reflective layers, a hard, on/off loss can be applied. Specifically, we model the building blockage as  $L_B = +\infty$  if the ray is obstructed, or  $L_B = 1$  otherwise.

Factoring in these elements, the overall loss for ray j is

$$L_{i} = L_{fs,i} L_{R,i} L_{A,i} L_{B,i}. \tag{11}$$

Fig. 3b shows the different contributions to the path loss at  $f_c = 178$  GHz for a satellite at 400 km of altitude, for different apparent look-angles  $\alpha_s$ .

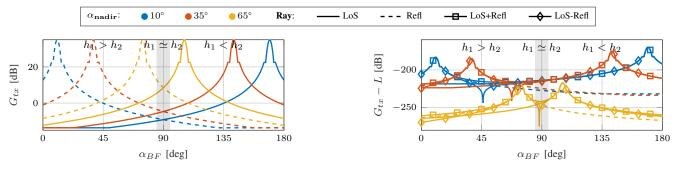
## C. Ray combining

Considering the propagation of a generic electric signal  $E_s \in \mathbb{C}$  from the source to the receiver, the signal E at the receiver antenna is given by the superposition of the electric fields of the LoS and ground-reflected rays

$$E = \sum_{j=0,1} E_{j} = \left(\frac{E_{s}e^{j2\pi\tau_{0}f_{c}}}{L_{B,0}L_{fs,0}L_{A,0}} + \frac{E_{s}e^{j2\pi\tau_{1}f_{c}+\phi_{R}}}{L_{B,1}L_{fs,1}|L_{R}|L_{A,1}}\right)$$

$$= E_{s}e^{j2\pi\tau_{0}f_{c}}\left(\frac{1}{L_{B,0}L_{fs,0}L_{A,0}} + \frac{e^{j2\pi\frac{\Delta d}{\lambda}+\phi_{R}}}{L_{B,1}L_{fs,1}|L_{R}|L_{A,1}}\right)$$

$$\simeq \frac{E_{s}}{L_{fs,0}L_{A,0}}e^{j2\pi\tau_{0}f_{c}}\left(\frac{1}{L_{B,0}} + \frac{e^{j2\pi\frac{\Delta d}{\lambda}+\pi}}{L_{B,1}|L_{R}|}\right)$$
(12)



(a) Beamforming gain of the terrestrial transmitter in the direction of the satellite as seen by the LoS and by the reflected ray, for different beamforming elevation angles  $\alpha_{BF}$ .

(b) Path loss to the satellite. LoS+Refl and LoS-Refl represent the bound for constructive and destructive interference, respectively.

Fig. 4: The ground reflection to the satellite is amplified by the main lobe of the gNB pointing towards the UEs and thus to the ground.

where  $\Delta d=d_1-d_0>0$  is the difference between the length of the two paths; and  $f_c$  and  $\lambda=\frac{c}{f_c}$  are the central frequency and the wavelength of the signal.

The approximations  $L_{fs,0}=L_{fs,1}$  and  $L_{A,0}=L_{A,1}$  are justified by the fact that for very long propagation distances, e.g., when considering the transmission from the ground to the satellite, the difference in path length  $\Delta d$  is small, making the atmospheric and the free-space losses experienced by the two rays almost equal. On the contrary, this kind of approximation does not hold in general for the phase. This is particularly true when considering high frequencies/short wavelengths, as the two rays are in phase opposition when  $\Delta d=2k\frac{\lambda}{2},k\in\mathbb{N}$ , i.e., a path difference of  $\frac{\lambda}{2}$ , in the order of millimeters or less for frequencies above 100 GHz, determines whether the rays combine constructively or destructively.

#### IV. SINGLE LINK ANALYSIS

In this section, we present a brief geometry-based analysis of the problem, that serves as the basis for the simulation setup, considering a single terrestrial link and an incumbent EESS. We analytically demonstrate that (i) reflections play a significant role in the RFI analysis, and that (ii) narrow beams, while successfully suppressing the direct interference, might amplify the undesired interfering multipath components.

The two factors that come into play when considering the propagation of electromagnetic waves at such high frequencies are (i) their interaction with the environment, described by the propagation model introduced in Sec. III, and (ii) the spatial distribution of the power, determined by the radiation and beamforming patterns of the antennas.

Prior work on RFI to satellite systems [4], [7] shows, often adopting a LoS channel model, that the narrow beamforming used in mmWave and sub-TeraHertz (sub-THz) networks can reduce enough the power that leaks in the direction of the passive user so as not to cause any significant interference. However, due to the particular geometry of the ground-to-satellite interference, represented in Fig. 2, reflections can not be neglected. In this section, we start by analyzing the geometry of a single link in Sec. IV-A to show that the power received through the ground reflection—accounting for propagation and beamforming—is not negligible, and comparable to the LoS ray in some cases. We then derive the corresponding probabilities for a single link in Sec. IV-B, and

provide some considerations on the impact of the frequency band in Sec. IV-C.

## A. Beamforming Amplification

Consider the link between a Transmitter (TX) and a Receiver (RX) with heights  $h_{tx}$  and  $h_{rx}$ , respectively, placed in the area illuminated by a passive EESS satellite with altitude  $h_s$ . We define the elevation beamforming angle  $\alpha_{BF}$  as the angle between the direction of the beamforming steering angle and the ground. In the following, we consider geometric beamforming, i.e., the beams of the TX and of the RX are aligned to the LoS connecting the two, with an inclination  $\alpha_{BF} = \alpha_{tx,rx}^{LoS}$ , and  $\theta_{HB}^{V}$  Half Power Beamwidth (HPBW).

For simplicity, we assume that the nodes and the satellites are aligned and consider the 2D geometry. Assuming that  $h_s \gg h_{tx}, h_{rx}$ , the LoS and the reflected rays emitted by the ground nodes are both amplified with gain  $G_S$  by the main lobe of the satellite sensor, due to the angular spread [36]. For this reason, in this analysis, we omit it and focus on the beamforming gain of the TX node  $G_{TX2S}$  toward the satellite.

To evaluate the interplay between the beamforming and the two rays, we consider three representative satellite nadir angles  $\alpha_n = \{10^\circ, 35^\circ, 65^\circ\}$ . The TX is equipped with an antenna array with a 3° HPBW and points towards the LoS to the RX. The path losses of the GR and the LoS ray are considered separately and combined destructively and constructively. The full elevation range of the beamforming angle is considered, from 0° (RX right below the TX) to 180° (RX above the TX). Fig. 4a shows how the transmitter beamforming gain  $G_{TX2S}$  amplifies the LoS (solid) and the reflected ray (dashed) as the beamforming angle changes. From Eqs. (2) and (4), the angular separation between LoS and ground reflection is  $\alpha_{tx.s}^{LoS} - \alpha_i \simeq \pi - 2\alpha_s$ . Thus, the only case when both rays are amplified is when  $\alpha_{tx,s}^{LoS} - \alpha_i < \theta_{HB}^V \implies \frac{\pi - \theta_{HB}^V}{2} < \alpha_s$ . Considering the narrow beams that will be adopted at these frequencies, this can happen only when both the satellite and the beamforming direction are at the horizon. However, as mentioned in Sec. III-A, we only consider satellite angles  $\alpha_s$ below 80°, thus excluding this case.

We can distinguish three behaviors, according to the geometric characteristics of the link:

C1)  $\alpha_{BF} < 90^{\circ} (h_{tx} > h_{rx})$ : In this case, the TX focuses its beam towards the ground. This is generally the case for

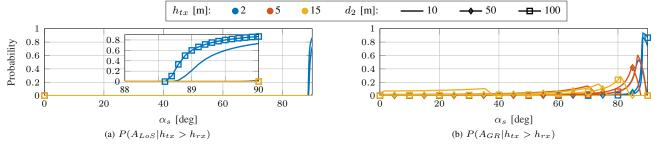


Fig. 5: Probability that the LoS  $(P(A_{LoS}))$  and the reflected  $(P(A_{GR}))$  rays are amplified by the main beam of the transmitting ground node.

the transmission from a gNB, placed in high locations for better coverage, to a UE at the ground level. Indeed, Fig. 4a shows that the LoS ray is effectively suppressed, particularly if the satellite is well above the horizon, whereas the ground reflection is greatly amplified.

- C2)  $\alpha_{BF} > 90^{\circ}$  ( $h_{tx} < h_{rx}$ ): Conversely, in this case, the transmitter points the beam upwards, as can be the case during the communication from a UE to a gNB. Here, the ground reflection is strongly attenuated and is negligible when compared to the LoS ray.
- C3)  $\alpha_{BF} \simeq 90^{\circ}$  ( $h_{tx} \simeq h_{rx}$ ): Here, the transmitter points at the horizon, e.g., to a node at similar height or very far away. We do not consider the latter, as at sub-THz frequencies the link length is short, whereas the former can be the case in Device-to-Device (D2D) communications or backhaul links. As mentioned above, the angular separation between the two rays makes it so that in this region neither of them is amplified.

In Fig. 4b, the overall amplification of each ray is obtained by subtracting the path loss L from the corresponding transmitter gain  $G_{TX2S}$ . The role of beamforming is extremely significant, as it can greatly amplify both the interfering rays, depending on the geometry. The peak power on the left side of Fig. 4b, i.e., when the ground ray is amplified (case C2), is lower than those on the right side (case C3), and their difference corresponds to the reflection loss. Finally, note that the superposition of the two rays is relevant only when they have similar amplitude and they have opposite phase (destructive). Specifically, when the TX beam amplifies the reflection enough to compensate for the reflection loss, the LoS and the reflected ray have comparable amplitude and cancel out. On the other hand, their constructive combination increases the aggregated power by at most 3 dB, when their phase is aligned and they have equal amplitude.

#### B. Probability of Beamforming Amplification

Starting from the considerations given in the previous section on the interfering power, we derive the probability of "beamforming amplification," identifying the events when the beam amplifies one of the two interfering rays, and the corresponding probabilities under some simplifying assumptions.

Let us consider only the vertical HPBW  $\theta^V_{HB}$  of the beam generated by TX. Let  $\alpha^{LoS}_{tx,s}$  be the angle between the horizontal direction at the TX and the LoS connecting the latter to the satellite. We define the event "the direct ray is amplified within the 3 dB range of the main lobe" ( $A_{LoS}$ , with

probability  $P(A_{LoS})$ ) as  $\frac{\theta_{HB}^V}{2} \geq |\alpha_{BF} - \alpha_{tx,s}^{LoS}|$ . Similarly, for the reflected ray, the event  $A_{GR}$  (with probability  $P(A_{GR})$ ) maps to the condition  $\frac{\theta_{HB}^V}{2} \geq |\alpha_{BF} - \alpha_i|$ , where  $\alpha_i$  is the reflection incident angle (Eq. (2)). Fixing the elevation angle of the satellite  $\alpha_s$ , from Eq. (2) and Eq. (4) we have:

$$(A_{LoS}): |\alpha_{BF}| \le \left(\alpha_{tx,s}^{LoS} \pm \frac{\theta_{HB}^{V}}{2}\right) \simeq \left(\pi - \alpha_{s} \pm \frac{\theta_{HB}^{V}}{2}\right) := \theta_{LoS}^{\pm}$$
(13)

$$(A_{GR}):$$

$$|\alpha_{BF}| \le \left(\alpha_i \pm \frac{\theta_{HB}^V}{2}\right) \simeq \left(\alpha_s \pm \frac{\theta_{HB}^V}{2}\right) := \theta_{GR}^{\pm}$$
(14)

The Probability Density Function (PDF)  $f_{tx,rx}^{LoS}\left(\alpha_{tx,rx}^{LoS}\right)$  of the LoS angles between the TX and the RX is fully characterized by the spatial distribution of the ground nodes. With the assumption of geometric beamforming, we can thus use the PDF of  $\alpha_{tx,rx}^{LoS}$ , easy to derive, in place of  $f_{BF}(\alpha_{BF})$ . Thus,

$$P(A_{LoS}) = \int_{\theta_{LoS}^-}^{\theta_{LoS}^+} f_{BF}(\alpha) d\alpha = \int_{\theta_{LoS}^-}^{\theta_{LoS}^+} f_{tx,rx}^{LoS}(\alpha) d\alpha$$
$$P(A_{GR}) = \int_{\theta_{GR}^-}^{\theta_{GR}^+} f_{BF}(\alpha) d\alpha = \int_{\theta_{GR}^-}^{\theta_{GR}^+} f_{tx,rx}^{LoS}(\alpha) d\alpha. \quad (15)$$

We can compute the LoS angle PDF starting from its Cumulative Distribution Function (CDF)  $F_{BF}$ , that can be derived from the distribution  $f_d$  and  $f_h$  of the TX-RX distance and of the node heights, respectively:

$$\alpha_{BF} = \arctan\left(\frac{d}{|h_{tx} - h_{rx}|}\right) := g(d, h_{tx}, h_{rx})$$

$$F_{BF}(\alpha) = \int_{D_{h_{tx}}} \int_{D_{h_{rx}}} \int_{D_{h_{d}}} f_{h_{tx}, h_{rx}, d} \left(h_{tx}, h_{rx}, d\right) dh_{tx} dh_{rx} dd$$

$$(17)$$

For simplicity, we can fix  $h_{tx}$  and limit our analysis to the case C1) identified in Sec. IV-A  $(h_{tx} > h_{rx})$  and assume that the height of the RX  $h_{rx}$  and its distance d from the transmitter are statistically independent. This is representative of a downlink communication from a gNB with known height  $h_{tx}$  to the served user at unknown distance d and height  $h_{rx}$ . Then, from Eq. (17)

$$F_{BF}(\alpha) = \int \int_{\alpha_{BF} < \alpha} f_{h_{rx},d}(h_{rx},d) \, \mathrm{d}h_{rx} \, \mathrm{d}d, \qquad (18)$$

which can be computed, if the distributions are known, by subsequently solving the two integrals using Eq. (16) to make a change of variable or using the method of transformations. We compute it for the TX-RX 2D distance d distributed uniformly in  $[d_1, d_2]$ , assuming that the links are established between non-overlapping nodes  $(d_1 > 0)$  within a maximum radius  $d_2$ , and  $h_{rx} \simeq U[h_1, h_2]$ ,  $0 < h_1 < h_2 < h_{tx}$ :

and 
$$h_{rx} \simeq U[h_1, h_2], \ 0 < h_1 < h_2 < h_{tx}$$
:
$$F_{BF}(\alpha) = \int_{h_1}^{h_2} \int_{d_1}^{\min(d_2, (h_{tx} - h_{rx}) \tan \alpha)} f_{h_{rx}, d}(h_{rx}, d) \, dh_{rx} \, dd$$

$$= \int_{h_1}^{h_2} (F_d(\min(d_2, (h_{tx} - h_{rx}) \tan \alpha))) \qquad (19)$$

$$-F_d(d_1)) f_{h_{rx}}(h_{rx}) \, dh_{rx} \qquad (20)$$

$$= \begin{cases} 0 & \text{if } 0^{\circ} < \alpha < \arctan\left(\frac{d_{1}}{h_{tx} - h_{rx}}\right) \\ \frac{\tan \alpha}{2\Delta d} \left(2h_{tx} - (h_{2} + h_{1})\right) \\ & \text{if } \arctan\left(\frac{d_{1}}{h_{tx} - h_{rx}}\right) < \alpha < \arctan\left(\frac{d_{2}}{h_{tx} - h_{1}}\right) \\ \frac{h_{tx} - h_{1} - d_{2}/\tan \alpha}{\Delta h} + \frac{\tan \alpha((d_{2}/\tan \alpha)^{2} - (h_{tx} - h_{2})^{2})}{2\Delta h \Delta d} \\ & \text{if } \arctan\left(\frac{d_{2}}{h_{tx} - h_{1}}\right) < \alpha < \arctan\left(\frac{d_{2}}{h_{tx} - h_{2}}\right) \\ 1 & \text{if } \arctan\left(\frac{d_{2}}{h_{tx} - h_{2}}\right) < \alpha < 90^{\circ}, \end{cases}$$

$$(21)$$

where  $\Delta h = h_2 - h_1$  and  $\Delta d = d_2 - d_1$ .

Then, the probabilities in Eq. (15) become, for the case under study,  $P(A_{LoS}|\text{C1}) = F_{BF}(\theta_{LoS}^+) - F_{BF}(\theta_{LoS}^-)$  and  $P(A_{GR}|\text{C1}) = F_{BF}(\theta_{GR}^+) - F_{BF}(\theta_{GR}^-)$ . Fig. 5 reports their value for different satellite elevation angles  $\alpha_s$  and  $\theta_{HB}^V = 3^\circ$ . As expected, for case C1), where  $h_{tx} > h_{rx}$ , the probability of amplifying the GR ray is greater than the corresponding one for LoS. Specifically,  $P(A_{LoS}|\text{C1})$  is not negligible only for the edge case when the satellite is at the horizon  $(\alpha_s \simeq 90^\circ)$  and the TX's height is comparable to that of the RX  $(h_{tx} = 2 \text{ m})$ . On the contrary,  $P(A_{GR}|\text{C1})$  is significantly larger

- when the satellite is above the ground nodes ( $0^{\circ} < \alpha_s \le 37.5^{\circ}$ ) and the TX is much higher than the RX ( $h_{tx} = 15$  m), that is within 10 m;
- when the satellite is between  $37.5^{\circ}$  and  $75^{\circ}$  and the TX is much higher ( $h_{tx} = 15$  m) than an RX within 10 m;
- when the satellite is at the horizon ( $\alpha_s > 80^{\circ}$ ). In this case, the ground reflection is less representative of practical cases, as explained in Sec. III-A.

The derivation for cases C2 and C3 is analogous.

## C. Frequency

In this section, we analyze a basic example to show how the carrier frequency  $f_c$  affects the interference to the satellite. Specifically, we consider a ground node placed at height  $h_{tx}=3$  m and a satellite at 400 km of altitude and  $\alpha_n=35^\circ$ , with antenna gains of 35 dB and 38.5 dB and HPBWs of 3° and  $2^\circ$ , respectively. In Fig. 6 we report the interference to the

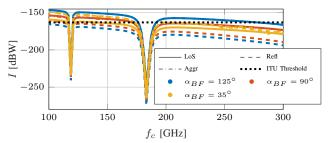


Fig. 6: Interference to the satellite for different Sub-THz frequencies. The satellite is at  $\alpha_n=35^\circ$  and at 400 km of altitude.

satellite for different frequencies, considering the LoS and the GR separately, as well as their superposition. For the ground node, we considered three beamforming angles, 90° (horizon, case C3), 125° (upwards, case C2), and 35° (downwards, case C1). The power of each ray is computed by combining the path loss L derived in Eq. (11) with the transmitter and satellite gain  $G_{TX2S}(\theta_{AoD}, \phi_{AoD})$  and  $G_S(\theta_{AoA}, \phi_{AoA}) = G_S$  of the TX and RX at the Angle of Departure (AoD) and Angle of Arrival (AoA), respectively:

$$I_{LoS} = P_{tx} + G_{TX2S}(\theta_{AoD}^{LoS}, \phi_{AoD}^{LoS}) + L_{LoS} + G_S$$
 (22)

$$I_{refl} = P_{tx} + G_{TX2S}(\theta_{AoD}^{refl}, \phi_{AoD}^{refl}) + L_{LoS} + G_S, \quad (23)$$

where  $P_{tx} = 0$  dBW. The power of the two rays is then combined according to Eq. (12).

First, we observe the presence of the two absorption peaks at 118 and 183 GHz, due to the presence of the oxygen molecules and of the water vapor, respectively. Secondly, we observe how the reflected ray can be amplified by the beam of the ground node, as explained in Sec. IV-A. Specifically, when the beamforming angle is  $125^{\circ}$ , the LoS ray is amplified, whereas the reflected ray is attenuated, and viceversa when the beamforming angle is  $35^{\circ}$ . Furthermore, we observe that, in the considered frequency band, the reflection loss remains almost constant, whereas the LoS path loss increases with the frequency and dictates the overall trend.

Finally, the ITU threshold [37] is exceeded particularly for frequencies below the second absorption peak. The only exception is when the ground node steers its beam toward the satellite, thus amplifying the LoS ray.

According to this observation, we selected three frequencies for the remainder of this work, 164, 178, and 240 GHz, that are representative of the three regions of the spectrum, i.e., below, close to and above the oxygen absorption peak, respectively. Accordingly, for our simulations we selected two satellites that operate in those bands, i.e., TEMPEST-D [8] for the former two and the MLS instrument on board of the Aura mission [9] for the latter.

# V. SIMULATION SETUP

In this and the following section, we report the setup and results of an extensive analysis of the RFI in different scenarios. The mathematical analysis in Sec. IV-B allows us (i) to gain a deep understanding of the simulation results, identifying the most significant elements that contribute to the overall power that reaches an incumbent satellite. Further, we (ii) accurately quantify the RFI in a realistic and complex scenario. Finally,



Fig. 7: Map of Boston with interfering nodes ( $\lambda_g=10$ ). The red areas represent the coverage of each gNB ( $d_{MAX}=200$  m in the Urban scenario).

	gNB (Urban/Backhaul)	UE (Urban)
$P_{TX}$ [dBm]	10/30	10
$G_{MAX}$ [dB]	35	24.5
$\theta_{HB}$ [deg]	3	10
$N^{SEC}$	3	1
Height [m]	$\{3, 5, 8, 10, 15\}$	$\mathcal{U}([1.6, 1.8])$

TABLE I: Network parameters for the simulation campaign.

	TEMPEST [8]	Aura MLS [9]
$\theta_{HB}$ [deg]	1.68/1.72	0.066 [38]
$f_c$ [GHz]	164/178	24.5
Altitude [km]	400	705
Scan Mode	Conical	Limb
$I_{th}$ [dBW] [37]	-163	-194

TABLE II: Specifications of the considered satellites.

we (iii) provide useful insights and guidelines for the study and simulation of the RFI at Sub-THz frequencies, that will hopefully help the study and design of coexistence solutions.

#### A. Scenarios

For this analysis, we consider two representative outdoor scenarios, the *Urban Cellular* and the *Backhaul* scenarios, both set in the city of Boston, MA, USA. The two present inherently different characteristics, e.g., different types of nodes and beamforming angle distributions, thus producing different interference patterns.

- 1) Map: We use data from the city of Boston to (i) select realistic locations for the terrestrial nodes and to (ii) characterize the path obstruction from the terrestrial network to the satellite. To do that, we extract terrain data and the road network from OSM using OSMnx [39] to reject the nodes spawned in invalid locations (e.g., on water surfaces) and to move indoor nodes outside the building footprint, respectively, as explained in the following paragraphs. To analyze the obstruction of the paths from the terrestrial network to the satellite, we used the 3D model of the buildings published by the Boston Planning & Development Agency<sup>1</sup>.
- 2) Node Characteristics: We define two types of nodes: the gNBs and the UEs (see Table I). The former represents a generic fixed node that can transmit using a large antenna array and thus a narrow beam ( $\theta_{HB}=3^{\circ}$ ). Each gNB has

 $N_{gNB}^{SEC}=3~120^{\circ}$ -wide angular sectors, according to the current 3rd Generation Partnership Project (3GPP) guidelines. The UEs represent mobile nodes with more limited beamforming capabilities ( $\theta_{HB}=10^{\circ}$ ). A single sector is available to the UE. For both gNBs and UE, in each sector a single link at a time can be active.

3) Node Placement: First,  $N_{gNB}$  tentative gNB locations are generated on the map according to a Poisson Point Process (PPP) with a given density  $\lambda_q$ . Then, the nodes are placed according to an iterative procedure loosely based on a Rejection Sampling process: the gNBs that overlap with the building footprint (i.e., indoor) or that are in invalid areas (e.g., water bodies) are projected to the nearest street using OSMnx [39]. The points for which this is not possible (e.g., the nearest street is an underground road, or two points overlap) are rejected, an equal number of new points are generated, and the procedure is iterated until all the nodes are successfully moved outside. Finally, for the Urban Cellular scenario,  $N_{UE}$  UEs are placed on the map with the same iterative procedure. According to [40], we deterministically set  $N_{UE} = N_{gNB} \times N_{gNB}^{SEC} \times 10$ . Thus, the number of nodes for each scenario is fully characterized by  $\lambda_a$ .

Three gNB densities were considered,  $\lambda_g \in \{10,45,100\}$  gNBs/km². In addition, we consider the number and location of gNBs that were approved by the City of Boston² as a fourth scenario named *Real*, with  $\lambda_g \simeq 18$  gNBs/km².

4) Attachment: In the Urban Cellular scenario, the UEs are assigned to gNBs according to the following algorithm: first, each UE is tentatively assigned to the closest gNB. If the distance d between the UE and the nearest gNB is larger than  $d_{max}=200\,$  m, the UE can not be served by any gNB and remains unattached, and the process is terminated. Otherwise, if the LoS between the UE and the gNB is unobstructed by the buildings, the assignment is confirmed and the process is terminated. If, on the contrary, the LoS is obstructed, the UE is assigned to the second-closest gNB, and the procedure is repeated from the distance-check step. Each UE in coverage is thus assigned a single gNB, and each sector of the gNB is assigned a list of UEs that it can serve.

In the Backhaul scenario, links are established between gNBs. First, a list with all the gNB pairs that are in LoS is computed. Then, for each link, a random direction for the data flow is picked. For each sector of the gNBs, a single link can be active at any given time.

5) Beamforming: The beam of each node is simulated using the ITU antenna pattern shown in Fig. 4a. The choice is justified both by the ITU recommendations and by computational efficiency, as computing the beamforming vectors and gains for the large areas and the corresponding number of nodes considered in this analysis is extremely demanding from a computational point of view. In both scenarios, geometric beamforming is considered, i.e., the beams of the TX and of the RX are aligned to the LoS direction connecting the two.

 $<sup>^1</sup>www.bostonplans.org/3d-data-maps/3d-smart-model/3d-data-download\\$ 

 $<sup>^2\</sup>mathrm{The}$  data is available in the Boston Open Data archive at https://tinyurl.com/2xjn9m43

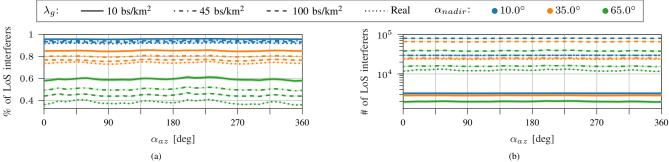


Fig. 8: Percentage (a) and number (b) of nodes not obstructed by the buildings for different satellite nadir angles and gNB densities, varying the satellite azimuth location.

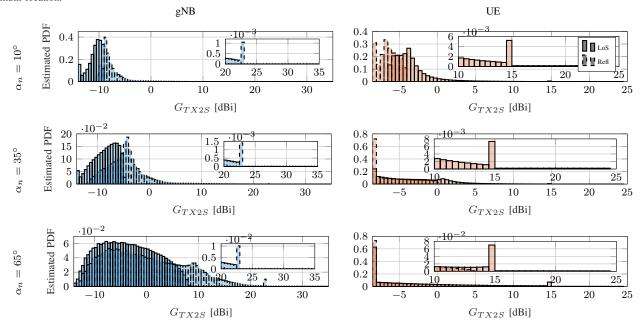


Fig. 9: Estimated PDF of the  $G_{TX2S}$  of the interfering rays for different satellite nadir angles in the Urban scenario.

#### B. Satellite Model

For the analysis, we consider a conical-scan and a limb radiometer. The conical scan mode sounds the Earth's surface, projecting its footprint on the ground. The limb scan mode views the edge of the atmosphere and terminates in space rather than at the surface. We model them using the specifications of the TEMPEST-D satellites [8] and of the MLS on the Aura mission [9]. The most relevant characteristics for this study are reported in Table II.

Given the importance of the geometry and of the obstruction by the buildings, we consider three representative nadir angles  $\alpha_n$ , as in Sec. IV, and sample the azimuth space  $\alpha_{az}$  with a sampling step of  $10^\circ$  for both satellites. Specifically, for a given nadir angle  $\alpha_n$ , the location of the satellite is determined by considering a conical scan and assuming that its main lobe is centered in the center of the considered area. That is, we fix  $\alpha_n$  and thus determine the horizontal x and the vertical distance  $h_{sat}$  from the center of the ground network, according to the geometry and notation shown in Fig. 1. The same location is also used for the limb satellite. However, for the RFI computation, the MLS main beam points 10 km above the network, while the TEMPEST one illuminates it, according to the respective scan mode.

## VI. NUMERICAL RESULTS

In this section, we present the results obtained through numerical simulations employing the setup presented in Sec. V. Specifically, in Sec. VI-A we report the results for the Urban Cellular scenario, evaluating the effect of the obstruction on the number of interfering nodes, the distribution of their gain, the aggregated power, the impact of different carrier frequencies and of different network load factors. Similarly, in Sec. VI-B we report the beamforming gain of the ground nodes toward the satellite and the aggregated interference of the backhaul network.

# A. Urban Cellular

a) Number of Interfering Nodes: Fig. 8a and Fig. 8b show the percentage and the number of ground nodes in LoS with the satellite, respectively, thus potentially interfering.

The x axis reports the azimuth of the satellite. Although the obstruction by the buildings plays a fundamental role, we can observe that the azimuth position of the satellite  $\alpha_{az}$  does not significantly affect the considered metrics, as the fluctuations are limited. This suggests that the building distribution is homogeneous in the azimuth domain, with some variations visible when considering large angles ( $\alpha_n \simeq 65^\circ$ ). Considering the percentage of (un)obstructed nodes allows us to draw

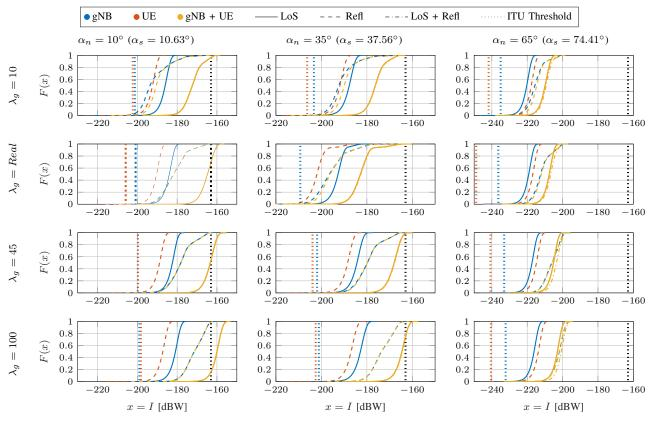


Fig. 10: Empirical Cumulative Distribution Function (ECDF) of the RFI power at the incumbent satellite, for different nadir angles and different gNB densities. For these results, we consider the TEMPEST satellite at 178 GHz.

conclusions that are independent of the absolute number of nodes. Fig. 8a shows that the percentage of ground nodes that can interfere with the satellite is strongly correlated to the nadir angle: when the satellite is above the city ( $\alpha_n \simeq 10^\circ$ ), the interfering signal propagates in the vertical direction, limiting the number of buildings that block it. Thus, almost 100% ground nodes are in LoS with the satellite. As the satellite moves towards the horizon, the percentage decreases, with almost 80% of the ground nodes able to reach it when it is at  $\alpha_n = 35^\circ$ , and as little as 50% when it is at  $\alpha_n = 65^\circ$ .

On the contrary, the absolute number of potential interferers reported in Fig. 8b is grouped by gNB density, as expected. However, the effect of the  $\alpha_n$  angle is still clearly visible, as for each density the number of potential interferers decreases as the satellite approaches the horizon.

b) Interfering Nodes Gain: As shown in Sec. IV-B, although the TX focuses the emitted power toward the RX through narrow beams, there is a non-zero probability that also the interfering rays to the satellite are amplified by the beamforming configuration of the TX. Fig. 9 reports the estimated PDF of the transmitter gain experienced by the interfering LoS and reflected rays that reach the satellite. For all the nadir angles, the vast majority of the rays are successfully suppressed  $(G_{TX2S} < 0)$ .

In particular, the UEs suppress the RFI with the minimum gain with high probability, corresponding to the peak probability in -8.5 dBi, that is clearly visible for  $\alpha_n=35^\circ$  and  $\alpha_n=65^\circ$ . On the contrary, the same behavior is not present when considering the gNBs, where a broader interval of  $G_{TX2S}$  has a high probability. This is due to the fact that the

interference, and hence the gain reported in Fig. 9, is computed only for the rays emitted by the angular sector containing the satellite. Given that the UEs have a single sector, all the rays are included for the PDF estimation, even when the antenna is pointing in the opposite direction. On the contrary, only the transmitter gain of the rays in the gNB sector containing the satellite is considered, based on the realistic assumption that the power leakage by a sector to the adjacent ones can be effectively suppressed. Thus, the gNB gains reported in Fig. 9 are computed only in the 120° angular sector containing the satellite instead of the whole 360° azimuth domain, thus increasing the probability of the antenna pointing toward the satellite in the azimuth plane.

Furthermore, Fig. 9 shows a distinct distribution for the LoS and for the ground-reflected rays when considering the gNBs and the UEs. Specifically, the LoS rays of the UEs have a greater probability of being amplified than the GR rays, and vice-versa for the gNBs. The zoom on the tails of the PDF highlights this behavior, with the highest gain being experienced by the GR (LoS) rays of the gNBs (UEs). This trend can be traced back to the analysis presented in Sec. IV-B: the UEs point upwards to the gNBs (case C2), amplifying the GR more than the LoS. Conversely, the gNBs point to the UEs and thus toward the ground, increasing the probability of amplifying the GR.

Moreover, all the estimated PDFs have multiple peaks, typical of the multimodal distributions. Again, referring to the analysis of Sec. IV-B, we can trace this behavior back to the discrete distribution of the gNB heights in relation to

_		$\alpha_n$ [deg]			$\alpha_n$ [deg]			$\alpha_n$ [deg]			
$m^2$		10	35		10	35			10	35	
s/k	10	0/0.0371/0.0368	0/0/0	10	0/0/0	0/0/0	1	0	0.0368	0	
9	45	0/0.4537/0.4537	0/0.012/0.012	45	8e - 4/0/7e - 4	1.5e - 4/0/1e - 5	4	5	0.4548	0.0148	
<u></u>	Real	0/0.3102/0.3102	0/1.85e - 4/1.71e - 4	Real	1.3e - 4/0/1.15e - 4	0/0/0	$R\epsilon$	al	0.3120	3.3e - 4	
6	100	0/0.8385/0.8385	0/0.2473/0.2469	100	0.0124/0/0.0124	0.0011/0/7.5e - 4	10	00	0.8415	0.27	
$\sim$	,										
		(a) LoS (gNB/UE/com	bined)		(b) Ground Reflection (gNB/	UE/combined)			<ul><li>(c) Aggrega</li></ul>	ited	

TABLE III: Probability that the RFI is greater than the ITU threshold for the cellular scenario, for the TEMPEST satellite at 178 GHz. For  $\alpha_n=65$  degrees, the probability is always 0.

the beam characteristics and the satellite positions. This favors some beamforming angles, and thus some  $G_{TX2S}$ .

Finally, also in this analysis, the elevation of the satellite plays a fundamental role. Firstly, we can observe the dramatic change in the shape of the distributions in the six plots of Fig. 9. For  $\alpha_n=10^\circ$ , both the LoS and the GR rays are strongly suppressed. Looking at Fig. 4a, this can be explained by the fact that the maximum amplification with this satellite elevation is obtained with extreme beamforming angles ( $\alpha_{BF}\simeq 10^\circ$  or  $\alpha_{BF}\simeq 172^\circ$ ), which are not common. On the contrary, when the satellite is at a lower elevation angle, the interfering LoS and GR rays are more often aligned with the beams, resulting in a more uniform distribution of the transmitter gain. However, a satellite at lower elevation angles also implies that terrestrial signals need to traverse a longer portion of the atmosphere, as we discuss next, and have a higher blockage probability, as discussed above.

c) Aggregated Power: Fig. 10 reports the ECDFs of the aggregated RFI power at the satellite for different nadir angles and for different gNB densities. For each Monte Carlo iteration, the total RFI is obtained by combining the electric fields at the receiver according to Eq. (12), thus accounting also for the phase difference. In particular, to analyze the different contributions to the overall power, we sum all the interfering power generated by the LoS (solid) and by the reflected (dashed) rays, aggregating the gNBs (blue) and of the UEs (orange). The LoS and reflected rays of the individual ground nodes are then combined according to Eq. (12) (dashdotted). Similarly, the overall RFI power (yellow) is obtained by combining all the aforementioned contributions. In each Monte Carlo iteration, we assume that all the gNB sectors either transmitting or receiving (with probability  $P_{TX}$  =  $P_{RX} = 0.5$ ) to a randomly selected UE among the one assigned to it. The sectors without assigned users remain silent.

First, we can observe that the power delivered by the LoS rays of the UEs to the satellite dominates the other contributions in almost all of the considered cases. This is due (i) to the fact that we consider a single gNB sector, as previously explained, as we assume that the gNBs can effectively suppress the inter-sector leakage. The same assumption does not hold for the UEs, due to the constantly-changing orientation of the hand-held devices. Furthermore, (ii) the UEs' beam amplifies their LoS ray to the satellite. On the contrary, the GR ray of the UEs is effectively suppressed. Conversely, the reflection from the gNBs to the satellite is stronger than the corresponding direct ray in almost all scenarios.

Secondly, as the satellite approaches the horizon, the overall RFI decreases. This is due to (i) the lower number of interfering nodes due to the obstruction by the buildings, as illustrated at the beginning of this section, and to (ii) the greater path

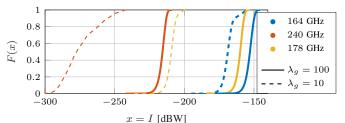


Fig. 11: Aggregated RFI observed by TEMPEST at 164 GHz and 178 GHz and by Aura at 240 GHz.

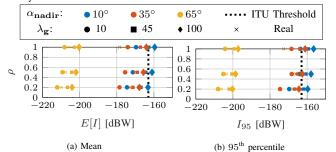


Fig. 12: Aggregated interference with different network load factors.

loss due to the larger distance of the satellite from the ground network. Furthermore, we observe that for higher nadir angles, the impact of the reflections is also increased, taking over that of the direct rays. Again, this is due to the considerations on the transmitter gain given in the previous paragraph.

Thirdly, we notice that, as expected, the overall RFI increases with the number of nodes. For reference, Fig. 8b reports the potential number of interferers for each density and nadir angle, although not all the nodes are simultaneously active. In Fig. 10, we report also the average interference generated by a single ground node (dotted). Note that the gap between the ECDF and the corresponding average interference is due to the aggregation of the RFI over the network. Considering the number in Fig. 8b, one might expect a larger difference, as we aggregate the power of several thousands of ground nodes, that would correspond to tens of dBs if we just summed the electrical field intensities at the satellite. However, due to the phase difference among the received signals, the overall interference is reduced, as a large percentage of signals superimpose destructively, canceling out.

Finally, Table III reports the probability that the total aggregated RFI at the satellite is greater than the ITU threshold for the acceptable RFI at the considered frequency ( $I_{th} = -163~\mathrm{dBW}$  [37]). The greatest interference is observed when the satellite is orbiting over the terrestrial network ( $\alpha_n = 10^\circ$ ) and with  $\lambda_g = 100~\mathrm{gNBs/km^2}$ . For the same satellite position, even as little as  $\lambda_g = 10~\mathrm{gNBs/km^2}$  is enough to cause significant interference to the satellite. On the contrary, when the satellite is at the horizon, the RFI is well below the safety levels.

d) Frequency: The results presented so far in this section were obtained considering  $f_c = 178$  GHz, where the propagation is characterized by a strong absorption by the atmospheric gases. Here, we compare the RFI observed by TEMPEST at 164 GHz, which is characterized by a lower absorption, at 178 GHz, and at 240 GHz, that is used by Aura. The results for the latter are analyzed in depth in the next paragraph. Fig. 11 reports the aggregated RFI for the three frequencies. Specifically, at 240 GHz it is well below the ITU threshold (-194 dBW for limb scanners), even when considering a high gNB density ( $\lambda_q = 100 \text{ gNBs/km}^2$ ) and  $\alpha_n = 10^{\circ}$ . Conversely, for 164 GHz, even when the RFI is the weakest ( $\alpha_n = 65^{\circ}$  and  $\lambda_q = 10$  gNBs/km<sup>2</sup>), it is above the threshold with a probability of 0.09. We can thus conclude that transmitting at frequencies close to the absorption peaks can indeed help mitigate the RFI, whereas transmitting in lower-absorption bands can almost certainly cause significant interference to conical-scan satellites.

e) MLS: As reported in Fig. 6, the RFI at the satellite antenna at 240 GHz can be higher than at 178 GHz. The large difference in interfering power observed in Fig. 11 is due to the different altitudes (705 km Aura vs 400 km TEMPEST) and scan modes of the satellites. While the TEMPEST satellite has a conical scanning sensor, the Aura satellite observes the limb layers of the atmosphere. Thus, the beam of TEMPEST amplifies the interference coming from the ground with maximum gain, whereas the MLS strongly attenuates it.

f) Network Load Factor: In Fig. 12 we show the total RFI for different network load factors. We define the network load factor through the activation probability  $\rho$ , which determines whether a gNB sector is active, i.e., on average a fraction  $\rho$  of the possible communication links is active. For instance, the aggregated interference reported in Fig. 10 assumes that all the gNB sectors are active (either transmitting or receiving), corresponding to  $\rho=1$ . Fig. 12 shows the mean and the 95<sup>th</sup> percentile of the aggregated RFI for  $\rho\in$ 

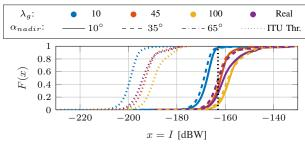


Fig. 14: Distribution of the aggregated RFI in the Backhaul scenarios.

 $\{0.2, 0.5, 1\}$ . A load factor of 0.2 or 0.5 effectively decreases the average interference E[I] below the ITU threshold for all the considered scenarios. Conversely, the 95<sup>th</sup> percentile  $I_{95}$  is less affected, remaining above the threshold when considering high density ( $\lambda_g = 45,100 \text{ gNBs/km}^2$ ) and small nadir angles ( $\alpha_n$ =10°). Note that Sub-THz networks with ultra-wide bandwidths are more likely to operate in scenarios with a small  $\rho$ , as transmissions can leverage high data rates and thus occupy the channel for reduced periods of time [1].

## B. Backhaul

a) Interfering Nodes Gain: For the backhaul scenario, links are established between gNBs, i.e., between nodes at similar heights. Thus, the transmitting beams are generally more aligned to the horizontal axis than those of their cellular counterpart. This behavior can be clearly observed in Fig. 13, where the histogram for the transmitter gain is reported, considering the TEMPEST satellite. We can observe how, due to the horizontal orientation, the beamforming effectively suppresses the interference, particularly when the satellite is above the network area ( $\alpha_{BF} \in \{10^\circ, 35^\circ\}$ ). As it lowers toward the horizon, larger gains become more probable. Furthermore, for the same reason, the gain of the LoS and reflected rays present almost the same distribution.

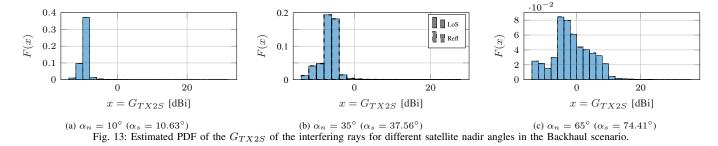
b) Aggregated Power: Fig. 14 reports the ECDF of the aggregated RFI in the considered scenarios, for the TEMPEST satellite at 178 GHz. We can observe that the aggregated power here is much greater than in the cellular scenario. This is mainly due to the increase in the transmitting power, which shifts all the distributions by about 20 dB.

The probability of exceeding the threshold in the different scenarios is reported in Table IV. Comparing it with the results reported in Table III, we can observe how the backhaul scenario generates much greater interference than the Urban Cellular one.

In conclusion, although the narrow beams suppress the power leaking toward the satellite, a backhaul network with the considered frequency can be potentially harmful to the incumbent satellites.

	$\alpha_n$ [deg]				
	10	35	65		
10	0.023	0.028	0		
45	0.655	0.527	0		
Real	0.74	0.527	0		
100	0.9138	0.872	0		

TABLE IV: Probability that the RFI is greater than the ITU threshold for the Backhaul scenario.



#### VII. CONCLUSIONS AND FUTURE WORKS

In this paper, we introduced analytical and simulation methodologies for the evaluation of RFI that next-generation terrestrial networks may introduce in passive sensing satellite systems. We developed a single-link analysis that shows the effect of beam amplification through the combined effect of the problem geometry, of the beam of the terrestrial TX and of the satellite. We then extended this into a large-scale data-driven simulation which relies on topologies for networks and buildings based on real-world data. The results show that—despite the high propagation and absorption loss at sub-THz frequencies—it is possible to generate RFI above ITU thresholds with specific network and satellite configurations.

These insights provide a foundation for our future work, which will focus on developing coexistence methods in a realistic data-driven framework. In addition, we will further extend our analysis by considering models for how RFI propagates into the passive sensors measurements.

#### REFERENCES

- I. F. Akyildiz, C. Han, Z. Hu, S. Nie, and J. M. Jornet, "Terahertz band communication: An old problem revisited and research directions for the next decade," *IEEE Trans. on Communications*, vol. 70, no. 6, pp. 4250–4285, Jun. 2022.
- [2] ITU, "Attenuation by atmospheric gases and related effects," Rec. ITU-R P.676-13, 2022.
- [3] V. Petrov, T. Kurner, and I. Hosako, "IEEE 802.15.3d: First Standardization Efforts for Sub-Terahertz Band Communications toward 6G," *IEEE Communications Magazine*, vol. 58, no. 11, pp. 28–33, Nov. 2020.
- [4] M. Polese, X. Cantos-Roman, A. Singh, M. J. Marcus, T. J. Maccarone, T. Melodia, and J. M. Jornet, "Coexistence and spectrum sharing above 100 GHz," *Proc. of the IEEE (to appear)*, 2023.
- [5] D. C. Kummerow et al., "Hyperspectral microwave sensors—advantages and limitations," *IEEE Journal of Selected Topics in Applied Earth Observations and Remote Sensing*, vol. 15, pp. 764–775, Dec. 2022.
- [6] M. Polese et al., "Dynamic spectrum sharing between active and passive users above 100 GHz," *Communications Engineering*, vol. 1, no. 1, p. 6, May 2022.
- [7] Y. Xing and T. S. Rappaport, "Terahertz Wireless Communications: Co-Sharing for Terrestrial and Satellite Systems Above 100 GHz," *IEEE Communications Letters*, vol. 25, no. 10, pp. 3156–3160, Oct. 2021.
- [8] S. Reising et al., "Overview of temporal experiment for storms and tropical systems (TEMPEST) CubeSat constellation mission," in *IEEE MTT-S International Microwave Symposium*. IEEE, 2015.
- [9] J.W. Waters et al., "The Earth observing system microwave limb sounder (EOS MLS) on the Aura Satellite," *IEEE Trans. on Geoscience and Remote Sensing*, vol. 44, no. 5, pp. 1075–1092, May 2006.
- [10] J. Park, E. Lee, S.-H. Park, S.-S. Raymond, S. Pyo, and H.-S. Jo, "Modeling and Analysis on Radio Interference of OFDM Waveforms for Coexistence Study," *IEEE Access*, vol. 7, pp. 35 132–35 147, 2019.
- [11] M. J. Marcus, "Harmful interference and its role in spectrum policy," Proc. of the IEEE, vol. 102, no. 3, pp. 265–269, Feb. 2014.
- [12] C. Bosso et al., "Ultrabroadband spread spectrum techniques for secure dynamic spectrum sharing above 100 ghz between active and passive users," in 2021 IEEE International Symposium on Dynamic Spectrum Access Networks (DySPAN), 2021, pp. 45–52.
- [13] F. Guidolin, M. Nekovee, L. Badia, and M. Zorzi, "A study on the coexistence of fixed satellite service and cellular networks in a mmWave scenario," in *IEEE International Conference on Communications (ICC)*, 2015, pp. 2444–2449.
- [14] C. Su, X. Han, X. Yan, Q. Zhang, and Z. Feng, "Coexistence Analysis between IMT-Advanced System and Fixed Satellite Service System," in IEEE Military Communications Conference, 2014, pp. 1692–1697.
- [15] A. J. Gasiewski, C. S. Ruf, M. Younis, and W. Wesbeck, "Impacts of mobile radar and telecommunications systems on Earth remote sensing in the 22-27 GHz range," in *IEEE International Geoscience and Remote Sensing Symposium*, vol. 3. IEEE, 2002, pp. 1679–1681.
- [16] W. A. Hassan, H.-S. Jo, and A. R. Tharek, "The Feasibility of Coexistence Between 5G and Existing Services in the IMT-2020 Candidate Bands in Malaysia," *IEEE Access*, vol. 5, pp. 14867–14888, 2017.

- [17] Ghaith Hattab et al., "Interference Analysis of the Coexistence of 5G Cellular Networks with Satellite Earth Stations in 3.7-4.2GHz," in *IEEE Int. Conference on Communications (ICC) Workshops*, 2018.
- [18] A. Alkhateeb, O. El Ayach, G. Leus, and R. W. Heath, "Hybrid precoding for millimeter wave cellular systems with partial channel knowledge," in *Information Theory and Applications Workshop (ITA)*. IEEE, 2013.
- [19] Liyuan Zhong et al., "The Feasibility of Coexistence between IMT-2020 and Inter-Satellite Service in 26 GHz band," in *Int. Wireless Communications and Mobile Computing (IWCMC)*, 2020, pp. 1006– 1011.
- [20] S. P. Winter and A. Knopp, "Statistics of Terrestrial Fixed Service Interference in the Aeronautical SATCOM Channel," in *IEEE International Conference on Communications (ICC)*, 2019.
- [21] Y. Cho, H. Kim, E. E. Ahiagbe, and H.-S. Jo, "Spectral Coexistence of IMT-2020 with Fixed-Satellite Service in the 27-27.5 GHz Band," in International Conference on Information and Communication Technology Convergence (ICTC), 2018.
- [22] Y. Cho, H. Kim, D. K. Tettey, K.-J. Lee, and H.-S. Jo, "Modeling Method for Interference Analysis between IMT-2020 and Satellite in the mmWave Band," in *IEEE Globecom Workshops*, 2019.
- [23] Y. Cho, H.-K. Kim, M. Nekovee, and H.-S. Jo, "Coexistence of 5G With Satellite Services in the Millimeter-Wave Band," *IEEE Access*, vol. 8, pp. 163618–163636, 2020.
- [24] R. Aghazadeh et al., "IMT to Satellite Stochastic Interference Modeling and Coexistence Analysis of Upper 6 GHz Band Service," *IEEE Open Journal of the Communications Society*, May 2023.
- [25] W. C. Jakes and D. C. Cox, Microwave mobile communications. Wiley-IEEE Press, 1994.
- [26] C. Han, A. O. Bicen, and I. F. Akyildiz, "Multi-ray channel modeling and wideband characterization for wireless communications in the terahertz band," *IEEE Trans. on Wireless Communications*, vol. 14, no. 5, pp. 2402–2412, Dec. 2014.
- [27] D. Kotz et al., "Experimental Evaluation of Wireless Simulation Assumptions," in *Proc. of the 7th ACM International Symposium on Modeling, Analysis and Simulation of Wireless and Mobile Systems*, Venice, Italy, 2004, p. 78–82.
- [28] F. Fund, R. Lin, T. Korakis, and S. S. Panwar, "How bad is the Flat Earth assumption? Effect of topography on wireless systems," in 14th International Symposium on Modeling and Optimization in Mobile, Ad Hoc, and Wireless Networks (WiOpt), 2016.
- [29] S. Loyka and A. Kouki, "Using two ray multipath model for microwave link budget analysis," *IEEE Antennas and Propagation Magazine*, vol. 43, no. 5, pp. 31–36, Oct. 2001.
- [30] M.J. Feuerstein et al., "Path loss, delay spread, and outage models as functions of antenna height for microcellular system design," *IEEE Trans. on Vehicular Technology*, vol. 43, no. 3, pp. 487–498, Aug. 1994.
- [31] M. Dottling, A. Jahn, D. Didascalou, and W. Wiesbeck, "Two- and three-dimensional ray tracing applied to the land mobile satellite (LMS) propagation channel," *IEEE Antennas and Propagation Magazine*, vol. 43, no. 6, pp. 27–37, Dec. 2001.
- [32] T. Soler and D. W. Eisemann, "Determination of look angles to geostationary communication satellites," *Journal of surveying engineering*, vol. 120, no. 3, pp. 115–127, Aug. 1994.
- [33] R. Piesiewicz, C. Jansen, D. Mittleman, T. Kleine-Ostmann, M. Koch, and T. Kurner, "Scattering analysis for the modeling of THz communication systems," *IEEE Trans. on Antennas and Propagation*, vol. 55, no. 11, pp. 3002–3009, Nov. 2007.
- [34] ITU, "Effects of building materials and structures on radiowave propagation above about 100 MHz," Rec. ITU-R P.2040-2, 2021.
- [35] K. Du, O. Ozdemir, F. Erden, and I. Guvenc, "Sub-Terahertz and mmWave Penetration Loss Measurements for Indoor Environments," in IEEE Int. Conference on Communications (ICC) Workshops, 2021.
- [36] F. Saggese, F. Chiariotti, K. Kansanen, and P. Popovski, "Efficient URLLC with a Reconfigurable Intelligent Surface and Imperfect Device Tracking," arXiv preprint arXiv:2211.09171, 2022.
- [37] ITU, "Performance and interference criteria for satellite passive remote sensing," Rec. ITU-R RS.2017-0, 2012.
- [38] R. Cofield and P. Stek, "Design and field-of-view calibration of 114-660-GHz optics of the Earth observing system microwave limb sounder," *IEEE Trans. on Geoscience and Remote Sensing*, vol. 44, no. 5, pp. 1166–1181, May 2006.
- [39] G. Boeing, "OSMnx: New methods for acquiring, constructing, analyzing, and visualizing complex street networks," Computers, Environment and Urban Systems, vol. 65, pp. 126–139, Sep. 2017.
- [40] 3GPP, "TR 38.913, Study on Scenarios and Requirements for Next Generation Access Technologies, V14.1.0," 2017.